

# In Situ Hydrothermal Conversion of Silica Gel Precursors to Binderless Zeolite X Pellets for Enhanced Olefin Adsorption

Hao Jiang<sup>1</sup>, Dan Wang<sup>1</sup>, Jialun Tan<sup>1</sup>, Yuxiang Chen<sup>1</sup>, Yang An<sup>1</sup>, Yonghao Chen<sup>1</sup>, Yuan Wu<sup>1</sup>, Hui Sun<sup>1</sup>, Ben-xian Shen<sup>1</sup>, Di Wu<sup>2</sup>, Jichang Liu<sup>1</sup>, Hao Ling<sup>1</sup>, Jigang ZHAO<sup>3</sup>, and Yujun Tong<sup>4</sup>

<sup>1</sup>East China University of Science and Technology

<sup>2</sup>Washington State University

<sup>3</sup>East China University of Science and Technology, Shanghai

<sup>4</sup>Sinopec Dalian Research Institute of Petroleum and Petrochemicals

May 5, 2020

## Abstract

Binderless zeolite X pellets were “one-pot” synthesized via in situ hydrothermal conversion of silica gel precursors in sodium aluminate solution. The conversion and crystallization kinetics were investigated as a function of synthesis time with a spectrum of techniques. It is found that four-membered (4R) and six-membered rings (6R) are formed by linking diffused Al species with dissolved Si species during the aging period, while the zeolite X frameworks are constructed via reorganization of  $\beta$  cages with double six-membered rings (D6R) in crystallization process. Furthermore, GCMC simulation was conducted to elucidate 1-hexene adsorption in zeolite X as ion species and exchange degree vary, in which adsorption capacity and guest – host interaction energy were evaluated. Incorporation of Mg<sup>2+</sup> and Ca<sup>2+</sup> enables higher adsorption capacity, while introduction of Co<sup>2+</sup>, Ni<sup>2+</sup>, Cu<sup>2+</sup> and Zn<sup>2+</sup> boosts adsorption and enhances interaction energy.

## Introduction

Effective separation of olefin/paraffin is critical for modern chemical industry,<sup>1-4</sup> in which olefins are primarily obtained from the hydrocarbons steam cracking mixtures to serve as feedstocks.<sup>5,6</sup> Removal of impurities from olefins must be maximized to ensure the high quality of subsequently derived-products.<sup>7,8</sup> Typical methods for olefin/paraffin separation include cryogenic distillation,<sup>3,9</sup> liquid – liquid extraction,<sup>10</sup> adsorptive separation,<sup>11-13</sup> and membrane separation.<sup>14-16</sup> Among all these approaches, adsorptive separation is considered to be a promising alternative compared to the current main technologies owing to its high selectivity and flexibility, mild operating condition and low capital cost.<sup>3,13,17</sup> Indeed, successful adsorptive separation largely relies on the performance of adsorbents employed. During the past several decades, a variety of porous materials, including aluminosilicate zeolites,<sup>12,18,19</sup> carbon molecular sieves,<sup>20,21</sup> and metal – organic frameworks (MOFs),<sup>22,23</sup> have been extensively explored, tested and applied for adsorptive separation of olefin/paraffin mixtures. Synthetic zeolites remain the most popularly utilized adsorbents in various industrial processes due to their high energetic and structural stability, and low cost.<sup>24,25</sup>

Ion-exchange has been primarily focused on tuning the pore structure and adsorption affinity to enhance adsorption capacity and selectivity.<sup>26,27</sup> According to earlier reports, a variety of ion-exchanged zeolite sorbents have been employed for selective adsorption of olefins over paraffins. Sakai *et al.*<sup>28</sup> reported that compared with the parent zeolite NaX membrane, the selectivity of Ag-exchanged zeolite X membrane for olefins increased from 3.63 (NaX) to 55.4 (AgX) for a propylene/propane (50:50) mixture. In addition, Anson *et al.*<sup>29</sup> studied the effect of cation type on the performance of ion-exchanged ETS-10 in ethane/ethylene

separation. They concluded that the adsorption selectivity of ethylene over ethane decreased following the order of  $\text{Na} > \text{K} > \text{Li} > \text{Cu}$  [?]  $\text{Ba} > \text{Ba/H} > \text{La/H}$ . This trend appears to be completely opposite to the pressure swing adsorption results. Moreover, it was reported that Cu-exchanged natural Chilean zeolite, which mainly consists of clinoptilolite and mordenite, showed increased number of adsorption sites and enhanced interaction energy in ethylene adsorption, which led to significantly increased adsorption capacity.<sup>30</sup>

For practical applications, conventionally synthesized zeolite powder has to be fabricated as macroscale particles/pellets with additional binder to ensure relative low pressure drop across the sorbent bed.<sup>31,32</sup> Nevertheless, the binder introduced is an adsorption inert component, which results in reduced adsorption capacity.<sup>31,33</sup> Moreover, the binder component may lead to undesired side reactions and/or diffusion inhibition.<sup>33,34</sup> To minimize the negative impacts of binder on the performance of industrial adsorbents, recently, we developed a one-pot route to synthesize binderless zeolite A pellets by using *in situ* hydrothermal transformation of silica gel precursors.<sup>35</sup>

In current work, we report synthesis of spherical binderless zeolite X pellets via *in situ* hydrothermal conversion of silica gel precursors. The synthesized binderless zeolite X exhibits significantly enhanced adsorption performance compared with commercially available binder-containing zeolite X products. Employing multiple analysis methodologies, we further characterized the resulting solid samples as the synthesis length varies and deduced the *in situ* conversion mechanism from precursors to zeolite X. Further, the impacts of ion type and exchange degree on olefin adsorption were evaluated experimentally by 1-hexene adsorption and computationally with GCMC simulation, in which we successfully correlate adsorption capacity and guest – host interaction energy with type of cation and degree of exchange for 1-hexene adsorption on ion-exchanged zeolite X.

## Experimental

### Materials

Sodium metaaluminate (> 98.5% purity), cetyltrimethyl ammonium bromide (CTAB, > 99.0 % purity) and binder-containing zeolite X-I were purchased from Aladdin Industrial Co., Ltd (Shanghai, China). Sodium hydroxide (> 96.0% purity), ammonium chloride (> 99.5% purity) and binder-containing zeolite X-II were provided by Sinopharm Chemical Reagent Co., Ltd (Shanghai, China). Silica sol (solid content of 40 wt%) with average particle size of 20 nm, was obtained from Qingdao Fuso Refining & Processing Co., Ltd (Qingdao, China). *n*-Heptane (> 99.0 % purity), binder-containing zeolite X-III and all nitrates (> 99.0 % purity) were supplied by Shanghai Titan Scientific Co., Ltd (Shanghai, China). Binder-containing zeolite X-IV was acquired from Nankai University Catalysts Co., Ltd (Tianjing, China). 1-Hexene (> 99.0% purity) was provided by Huawei Ruike Chemical Industry Co., Ltd (Beijing, China). Deionized water was applied in all synthesis experiments. All chemicals were used without further purification.

### Synthesis of binderless zeolite X pellets

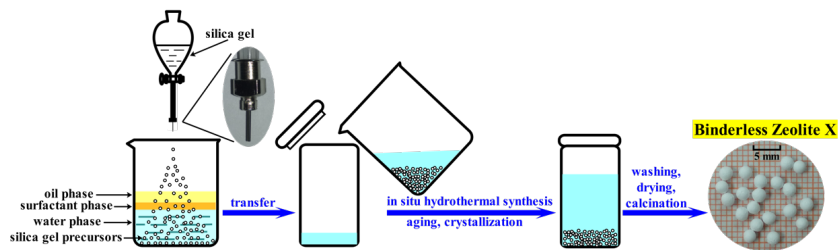


**Figure 1.** Schematics of *in situ* hydrothermal synthesis of binderless zeolite X pellets.

Binderless zeolite X pellets were prepared by modifying the method we reported earlier to synthesize zeolite A (see Figure 1).<sup>35</sup> First, a custom-made oil/water column for synthesis of the silica gel precursors was prepared. Specifically, the *water phase*: sodium aluminate alkaline solution (250 mL) was prepared by dissolving sodium metaaluminate (24.6 g) and sodium hydroxide (24 g) into deionized water (230 g). Saturated CTAB aqueous solution (15 mL) served as the *surfactant phase* while *n*-heptane (30 mL) was employed as the *oil phase*. These three phases were successively added in a beaker. Subsequently, the silica gel mixture, which was obtained by stirring the mixture of silica sol (45 g) and ammonium chloride solution (10 g, 10 wt%), was dripped into the aforementioned custom-made column through a 0.35 mm (id) syringe needle in order to form spherical silica gel precursors of 2~3 mm in size. Subsequently, the alkaline solution at the bottom as well as the silica gel precursors obtained were separated from the oil/water column followed by transfer to a Teflon-lined stainless steel autoclave. The molar composition of the prepared reaction system was  $3\text{Na}_2\text{O}:\text{Al}_2\text{O}_3:2\text{SiO}_2:98\text{H}_2\text{O}$ . After aging at 313 K for 0 to 6 h, the zeolite X products were crystallized at 373 K systematically for 0 to 24 h. Washing samples was triplicated with deionized water. The resulting products were collected through filtration and dried at 373 K overnight.

#### Ion-exchange of synthesized zeolite X pellets

Various ions were introduced into the synthesized zeolite NaX to obtain zeolite M-NaX. Particularly, 25 g zeolite NaX pellets were immersed into 250 mL  $\text{M}(\text{NO}_3)_x$  ( $\text{M} = \text{Mg}^{2+}, \text{Ca}^{2+}, \text{Co}^{2+}, \text{Ni}^{2+}, \text{Cu}^{2+}, \text{Zn}^{2+}$  and  $\text{Ag}^+$ ) aqueous solution (0.1 mol/L) under vigorous stir at 333 K for 6 h. The ion-exchanged zeolite X samples were washed with deionized water for three times, separated by filtration and dried in a vacuum oven at 373 K overnight.

#### Materials characterization

Powder X-ray diffraction (XRD) patterns of all samples were obtained by employing a Bruker D8 Advance X-ray diffractometer (Bruker AXS Inc., Germany) with Ni-filtered  $\text{Cu K}\alpha$  radiation ( $\lambda=1.5418 \text{ \AA}$ ) operated at 40 kV and 40 mA. The  $2\theta$  scanning angle recorded ranges from 5 to 60° with a step size of 0.02 and a rate of 5° per minute. All XRD patterns were analyzed using Jade 6.0 and ICSD database for phase identification. Furthermore, the relative crystallinity was evaluated.

The sample morphology was evaluated using a Nova NanoSEM 450 scanning electron microscope (SEM; FEI, USA) with an accelerating voltage of 15 kV and a beam current of 10 nA. Elemental analysis was carried out on a Falcon energy-dispersive spectrometer (EDS) (EDAX Inc., USA). A sputter coating with a thin layer of platinum was adopted to avoid charging. Six measurement points were selected at different positions to obtain the average elemental composition for each sample.

High resolution transmission electron microscopy (HRTEM) analyses were carried out on a JEM-2100 electron microscope (JEOL Co., Ltd., Tokyo, Japan) with an accelerating voltage of 200 kV. All samples were dispersed in absolute ethanol by ultrasonic treatment. Subsequently, the particle-suspended solution was dropped onto copper TEM grids coated with a holey carbon film and dried at room temperature.

The pore structure of each sample was measured by  $\text{N}_2$  adsorption at 77 K using a 3H-2000PM2 automatic surface analyzer (BeiShiDe Instrument Co., Ltd., Beijing, China). The specific surface areas, micropore and mesopore volumes were calculated using the Brunauer-Emmett-Teller (BET), Harvath-Kawazoe (H-K) and Barrett-Joyner-Halenda (BJH) method, respectively. Vapor adsorption of 1-hexene on zeolite X samples was determined under  $P/P_0=0.85$  at 298 K using a 3H-2000PW gravimetric vapor adsorption analyzer (BeiShiDe Instrument Co., Ltd., Beijing, China). All samples were outgassed at 573 K for 12 h prior to adsorption measurements.

Raman spectra were collected by using a Renishaw InVia Reflex Lase Micro-Raman Spectrometer (Renishaw Plc., U.K.) equipped with a 325 nm argon ion laser. Data were recorded from 1200 to 200  $\text{cm}^{-1}$  with a spectral resolution of 1.6  $\text{cm}^{-1}$  and using a grating of 2400 lines\* $\text{mm}^{-1}$ .

Solid-state  $^{29}\text{Si}$  and  $^{27}\text{Al}$  magic angle spinning nuclear magnetic resonance (MAS-NMR) spectra were recorded on a Bruker Avance-III 500 MHz super conducting Fourier NMR spectrometer (Bruker AXS Inc.,

Germany) with a 4 mm MAS probe. The chemical shifts of  $^{29}\text{Si}$  and  $^{27}\text{Al}$  MAS NMR were externally referenced to tetramethylsilane (0 ppm) and 1M  $\text{AlCl}_3$  aqueous solution (0 ppm), respectively.

#### Grand Canonical Monte Carlo (GCMC) simulation

All computation simulations were performed using Sorption module in Materials Studio 7.0 package (Accelrys Inc., USA). The adsorption of 1-hexene on different ion-exchanged zeolite X structures were calculated based on the Grand Canonical Monte Carlo (GCMC) and configurational bias methods with periodic boundary conditions.<sup>36</sup>

The parent FAU framework topology was obtained from the Materials Studio database. According to the compositions of synthesized samples determined by EDS analyses (see Table S1), the Al atoms were randomly replaced by Si atoms, automatically following the Lowenstein's Al-O-Al avoidance rule.<sup>37</sup> In addition, the corresponding extra-framework ion distribution was conducted by using the Locate Task in Sorption module,<sup>38,39</sup> which can avoid the choice of ion amount at a specific position caused by the exchange of ion species.<sup>40</sup> The structural models of ion-exchanged zeolite X samples were enabled by replacing  $n$   $\text{Na}^+$  cations with  $n/x$   $\text{M}^{x+}$  ones in unit cell based on the found compositions. Moreover, the extra-framework ions incorporated in the zeolite structures can be  $\text{Na}^+$ ,  $\text{M}^{x+}$ , or mixed cations. The Cartesian and fractional atomic positions were fixed during the simulation to restrict the adsorption in a specific region.

The 1-hexene module was built by a united-atom description, in which each  $\text{CH}_3$  ( $\text{sp}^3$ ),  $\text{CH}_2$  ( $\text{sp}^3$ ),  $\text{CH}$  ( $\text{sp}^2$ ), and  $\text{CH}_2$  ( $\text{sp}^2$ ) group was treated as a single interaction center with effective potential parameters.<sup>41</sup> Table S2 lists the Lennard-Jones 12-6 potential parameters of 1-hexene groups and partial charges of the zeolite X framework system we used.<sup>41,42</sup> The Lennard-Jones potential parameters for zeolite X was obtained using the COMPASS force field,<sup>43</sup> which has a wide application in prediction the covalent molecules adsorption on FAU zeolite.<sup>44,45</sup> During simulation, all bond lengths were considered to be rigid, while bond angles were allowed to bend. Interactions among different sites were computed based on the standard Lorentz-Berthelot combining rule, and all interactions were cut off at a radius of 12.5 Å and a cubic spline truncation of 1 Å width. The Ewald summation method was used to handle the electrostatic interactions between guest and host atoms with accuracy of 0.0001 kcal/mol. The guest – host potential energy and the density field of the guest molecules were sampled with 25 points between two evaluations of the field data on a three-dimensional grid of 0.25 Å spacing.

GCMC simulation was employed to calculate the adsorption capacity and van der Waals interaction energy. The temperature ( $T$ ), volume ( $V$ ) and chemical potential ( $\mu$ ) of the system were fixed, while the system energy ( $E$ ), pressure ( $P$ ) and total number of molecules ( $N$ ) varied. For each adsorption calculation point, the computational process was equilibrated during 5,000,000 steps and followed by 5,000,000 production steps for data collection. In order to validate the experimental results, the predicated simulation data were converted from absolute values to excess adsorption properties.

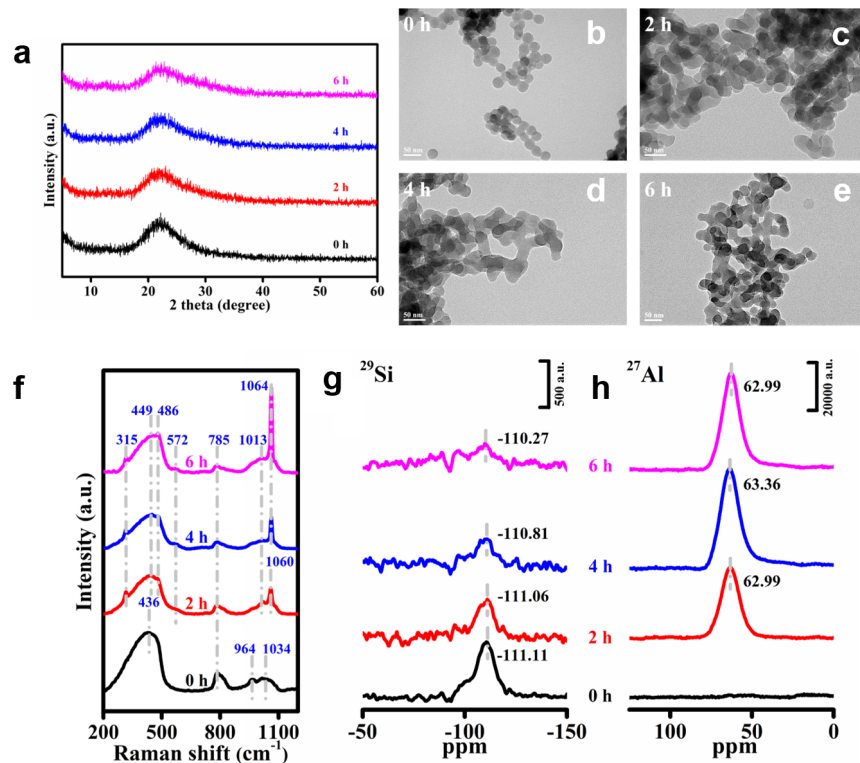


**Figure 2.** (a) XRD patterns, (b to e) TEM images, (f) UV-Raman and (g and h) NMR spectra of the % amorphous aluminosilicate precursors with different aging lengths.

## Results and Discussion

### Aging of amorphous aluminosilicate precursor

To understand the aging process of silica gel precursors in sodium aluminate alkaline solution, the as-synthesized samples with different aging times were characterized using integrated structural, microscopic and spectroscopic methods. According to the XRD patterns in Figure 2a, the initially prepared silica gel precursors at the aging time of 0 h exhibit to be completely amorphous, which suggests the existence of initial silica nanoparticles in the precursors. The TEM images (see Figures 2b– e) further confirm the presence of spherical silica nanoparticles (~20 nm) in the as-prepared precursors. The Raman bands at 436, 785, 964 and 1034  $\text{cm}^{-1}$  corresponding to the initial silica nanoparticles are observed in the Raman spectrum for the sample prior to aging (see Figure 2f). The broad band centered at 436  $\text{cm}^{-1}$  is assigned to the bending mode of the Si-O-Si bond.<sup>46</sup> The band at 785  $\text{cm}^{-1}$  can be attributed to the symmetric stretching mode of the Si-O-Si bond,<sup>46</sup> while the bands at 964 and 1034  $\text{cm}^{-1}$  are associated with the asymmetric stretching mode of the Si-O-Si bond.<sup>47</sup> Additionally, the  $^{29}\text{Si}$  MAS NMR spectrum in Figure 2g features a wide chemical shift at about -111.11 ppm, corresponding to the silica nanoparticles in the original silica gel precursors.<sup>35</sup> The absence of  $^{27}\text{Al}$  MAS NMR signal confirms a pure silica phase (see Figure 2h). Extended aging length leads to slight decrease in XRD peak intensity for amorphous silica, which is further supported by the TEM images clearly demonstrate the morphological transformations of silica nanoparticles in the sodium aluminate alkaline solution during the aging process. Specifically, as the aging length increases the dispersed silica nanoparticles gradually become coral-like amorphous aggregates without further crystallization. Such phenomenon is consistent with the XRD results showing no evidence of long range order.

As the aging time reaches 2 h, several weak Raman bands are detected in the region of 300 to 600  $\text{cm}^{-1}$ , which correspond to different ring sizes.<sup>48,49</sup> The bands at 315 and 486  $\text{cm}^{-1}$  can be ascribed to the bending modes

of the T-O-T bond of the 6R and 4R, respectively, which indicate the formation of secondary building units (SBUs).<sup>50</sup> The 4R suggested by the Raman band at 486  $\text{cm}^{-1}$  is probably dissociative, which is distinctly different from the rings in zeolite X structure at around 500  $\text{cm}^{-1}$ . The band at 572  $\text{cm}^{-1}$  is associated with the Al-O-Si stretches of the aluminosilicate anions formed in alkaline solution.<sup>51</sup> Moreover, the bands at 436, 964 and 1034  $\text{cm}^{-1}$  (for the original precursor sample) shift to 449, 1013 and 1060  $\text{cm}^{-1}$  (for the sample at 2 h of aging time), respectively. Extended aging length leads to stronger Raman absorption at 486 and 1060  $\text{cm}^{-1}$ , indicating gradual formation of 4R and T-O-T bonds during the aging process, respectively.

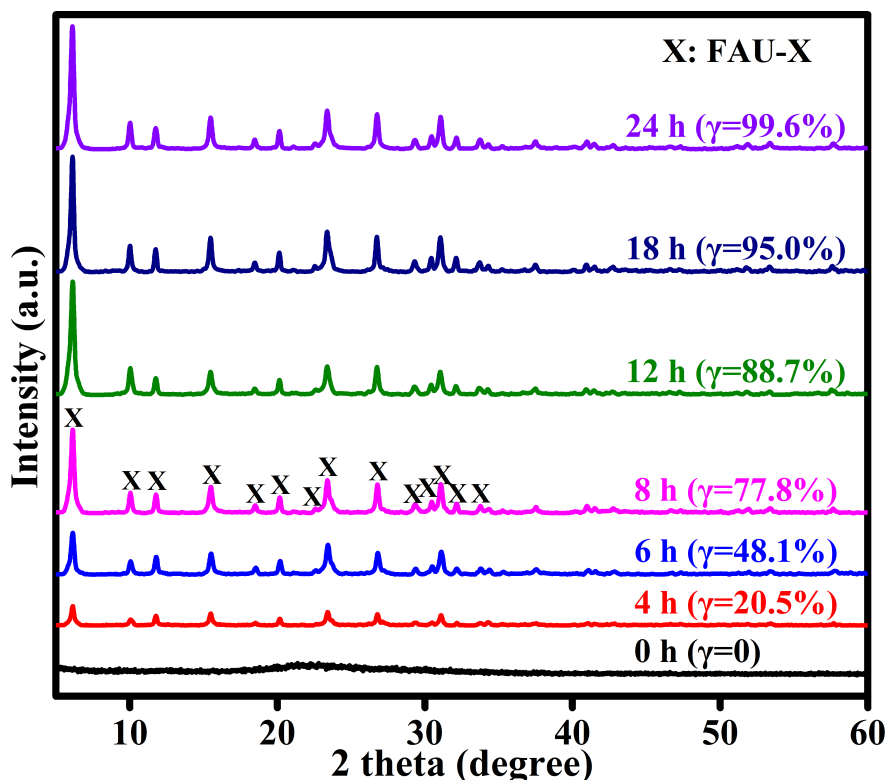


**Figure 3.** XRD patterns of the synthesized samples at different crystallization times.

In the  $^{29}\text{Si}$  MAS NMR spectra, the chemical shift at around -111 ppm gradually vanishes during the aging process because of the conversion of silica nanoparticles to aluminosilicate species. The  $^{27}\text{Al}$  MAS NMR spectra show a chemical shift centered at  $\sim 63$  ppm suggesting multiple chemical circumstances of Al species with the Al atom binding to different number of -O-Si- groups. As the aging time increases, the intensity of the peak at  $\sim 63$  ppm increases, indicating continuous gelation of -O-Si- groups of silica precursors binding to Al species within the sodium aluminate alkaline solution. Such reaction is primarily dominated by the diffusion of Al species into the silica gel precursor pellets. Interestingly, for all samples collected during aging, there is no characteristic Raman band corresponding to the D6R of zeolite X framework. We conclude that there is probably no crystalline phase formed during the aging process, and all samples appear to be completely amorphous, evidenced by the XRD and TEM results.

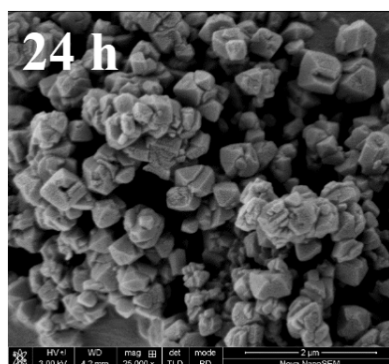
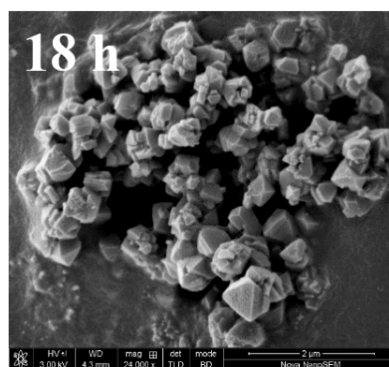
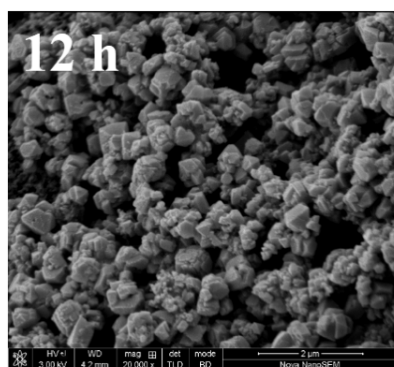
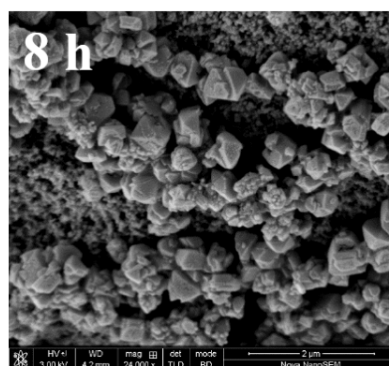
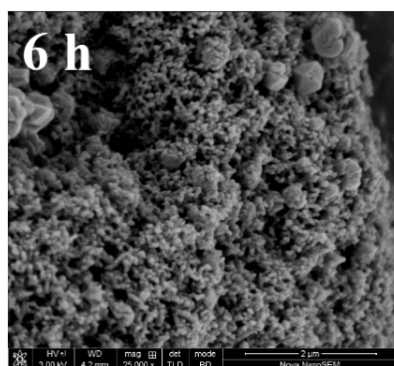
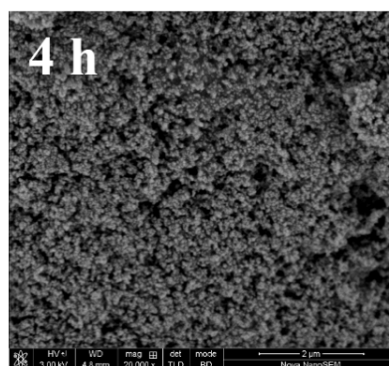
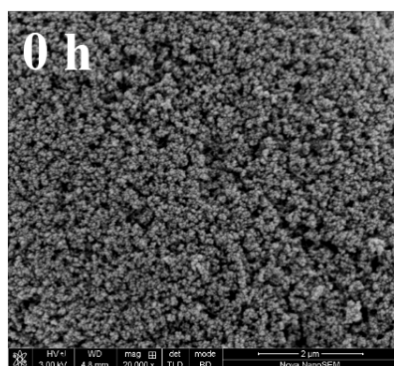


**Figure 4.** SEM images of the synthesized samples at different crystallization times.

#### Crystallization of zeolite X

After aging, hydrothermal treatment was applied on the same reaction system (reactor) with amorphous aluminosilicate precursors to crystallize zeolite X at elevated temperature. To reveal the compositional and structural evolutions the precursors undergo during *in situ* conversion to zeolite X, samples with different crystallization times ( $t_c$ ) were collected and thoroughly characterized with structural, spectroscopic and microscopic methods. Specifically, when  $t_c = 4$  h, preliminary phase transition from the amorphous aluminosilicate aggregates to zeolite X crystals was observed (20.5 % relative crystallinity) according to the XRD data shown in Figure 3. The morphological changes of crystallization initiated from the gel precursors are revealed by SEM and TEM images presented in Figures 4 and 5 respectively. It appears that the silica nanoparticles become denser aggregates, and partially-crystallized particles from these aggregates were observed at  $t_c = 4$  h.

The Raman bands at 290, 366, 504, 1000 and 1063  $\text{cm}^{-1}$  (see Figure 6a) belonged to the framework structure of zeolite X are detected at  $t_c = 4$  h.<sup>52</sup> Specifically, the sharp band at 504  $\text{cm}^{-1}$  is assigned to the bending mode of T-O-T bond of the 4R in the zeolite X structure.<sup>50</sup> The double bands at 290 and 366  $\text{cm}^{-1}$  can be attributed to the bending modes of T-O-T bond of D6R, which indicate initial crystallization of zeolite X. In contrast, the absence of these signals for sample at  $t_c = 0$  h strongly suggests no zeolite X formation. Additionally, the bands at 1000 and 1063  $\text{cm}^{-1}$  are ascribed to the asymmetric stretching vibration modes of the T-O-T bonds in zeolite X framework.<sup>50</sup> Moreover, the Raman results also suggested formation of second structure units of 4R, 6R and D6R when  $t_c = 4$  h, implying the existence of ordered crystalline zeolite X framework.

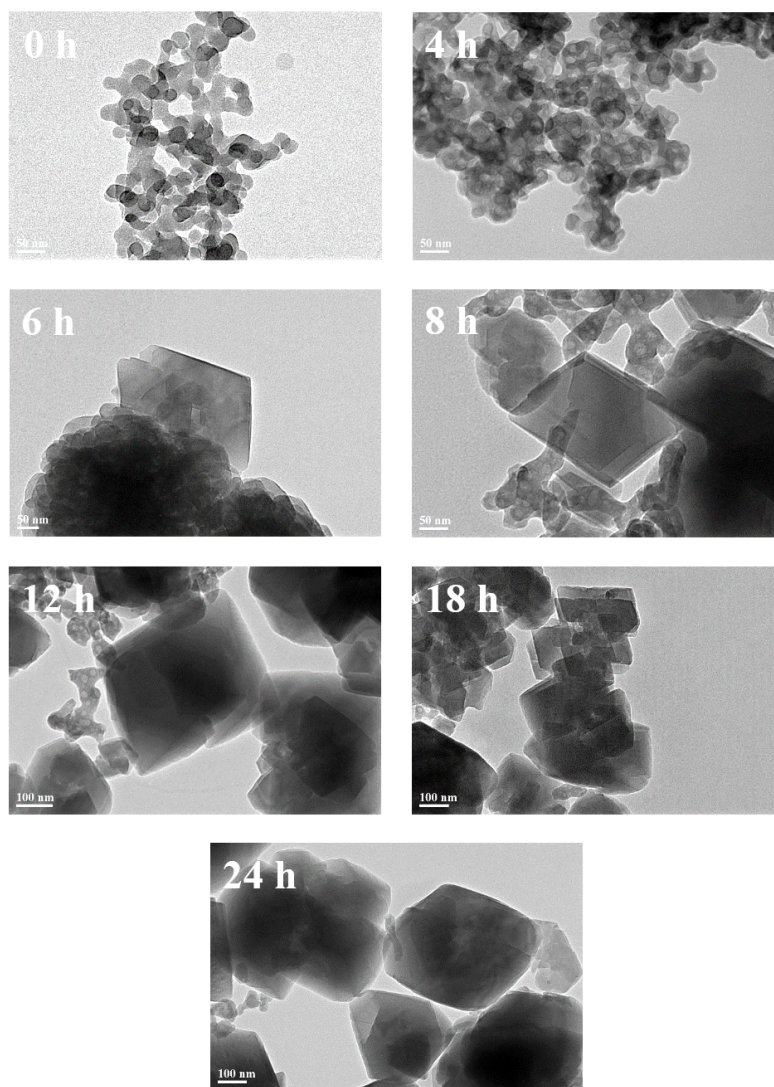


**Figure 5.** TEM images of the synthesized samples at different crystallization times.

The  $^{29}\text{Si}$  MAS NMR spectrum of the sample with  $t_c$  of 4 h presents chemical shifts at  $\delta = -86.82, -91.00, -96.02$  and  $-100.44$  ppm (see Figure 6b), which correspond to the  $\text{Si}(\text{O-Al})_4$ -,  $\text{Si}(\text{O-Al})_3$ -,  $\text{Si}(\text{O-Al})_2$ - and  $\text{Si}(\text{O-Al})$ - (Si linking to different number of Al atoms by oxygen bridges) species, respectively.<sup>53</sup> The  $^{27}\text{Al}$  MAS NMR spectra shown in Figure 6c present significantly enhanced chemical shift at  $\sim 61$  ppm owing to the binding of Al intermediate species with different number of  $-\text{O-Si}-$  groups.<sup>35</sup>

On the other hand, the development of zeolite X phase was monitored by XRD as a function of crystallization time. First, characteristic patterns of zeolite X were confirmed for all samples investigated.<sup>54</sup> As crystallization proceeds, the relative crystallinity of zeolite X gradually increases until reaching the maximum at 24 h. Specifically, the samples with crystallization times of 6, 8 and 18 h have relative crystallinity of 48.1 %, 77.8 % and 95.0 %, respectively. Eventually, the relative crystallinity of sample crystallized up to 24 h is 99.6 %.

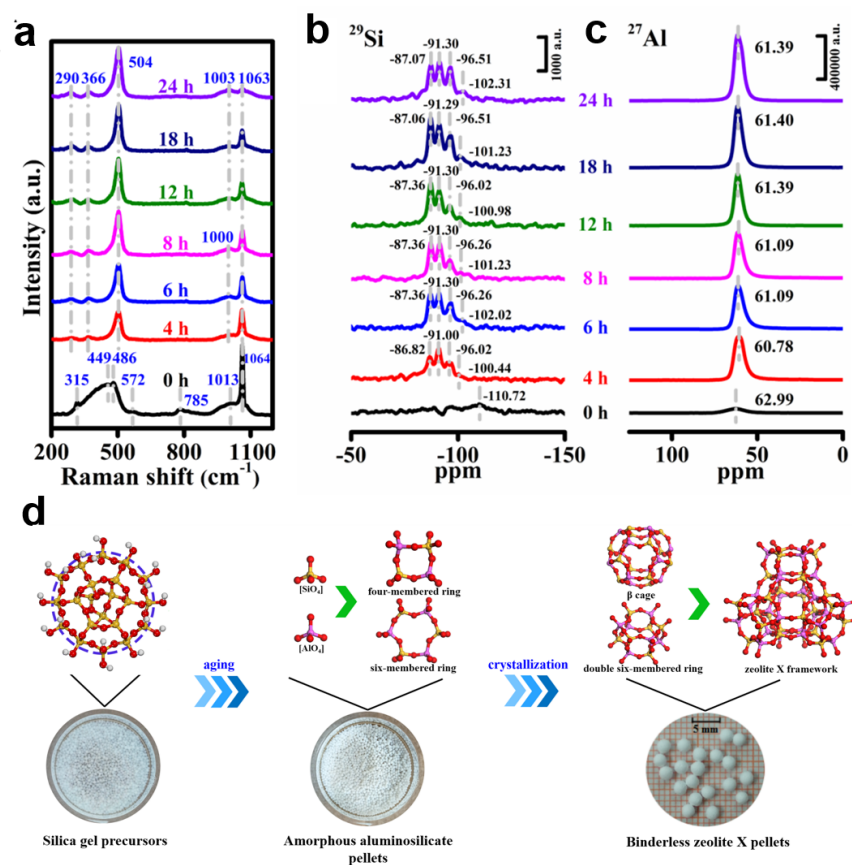


**Figure 6.** (a) UV-Raman and (b and c) NMR spectra of the hydrothermally synthesized samples with different crystallization times. (d) The mechanism deduced for in situ binderless zeolite X synthesis from silica gel precursors.

From the SEM and TEM images presented in Figures 4 and 5, at  $t_c = 8$  h, a number of crystals, from 300 to 500 nm in size, are observed within the gel precursors. This suggests the formation of zeolite X crystals accompanied by consumption of silica nanoparticles. Additionally, the Raman signals of 4R and D6R become stronger as crystallization time increases, clearly suggesting formation of zeolite X structure. Meanwhile, the chemical shift at about -96 ppm in the  $^{29}\text{Si}$  MAS NMR spectra becomes stronger as  $t_c$  increases suggesting increase of the  $\text{Si}(\text{O}-\text{Al})_2$  species population in the zeolite X framework. Moreover, all peaks in the  $^{29}\text{Si}$  and  $^{27}\text{Al}$  MAS NMR spectra retain their positions, while their intensities increase due to the increase of structural Si and Al species in zeolite X framework. According to these results, the formation of zeolite X framework is enabled through the self-aligned assemblage of the 4R, 6R and D6R, accompanied with consumption of Si species in the silica gel precursors and transportation of Al species to the silica gel pellets.

According to these results, we deduce the mechanism of *in situ* hydrothermal conversion of silica gel precursors to binderless zeolite X pellets (see Figure 6d). First, in the low temperature aging period, the precursors containing silica nanoparticles are converted to amorphous aluminosilicate aggregates by reacting with the Al species to form the primary building units of  $[\text{SiO}_4]$  and  $[\text{AlO}_4]$ , in which the Al species diffuse from the bulk solution to the silica gel precursors accompanied with simultaneous formation of second building units (4R and 6R). During the crystallization process, D6R are created by interconnection between 6R and 4R, while the  $\beta$  cages are developed via self-assemblage of the second building units. Finally, the zeolite X framework is constructed through the reorganization of  $\beta$  cages with D6R. In our study, all these transformations take

place *in situ* from the initial prepared silica gel precursors.

### Kinetic analysis of crystallization

To further understand the crystallization kinetics, the relative crystallinity of the synthesized samples is examined as a function of  $t_c$ . The aging time was fixed to be 6 h. The crystallization kinetic curve is well described by using the Avrami - Erofe'ev (A-E) expression (see Equation (1)).<sup>55,56</sup>

$$\gamma = [1 - \exp(- (k (\tau_c - \vartheta))^n)] \times 100\% \quad (1)$$

where  $\gamma$  is the relative crystallinity.  $k$  is the apparent rate constant of crystallization.  $t_c$  and  $\vartheta$  are the times of crystallization and induction, respectively. And  $n$  is the A-E exponent, a parameter related to the mechanism for nucleation and crystal growth.

By correlating the crystallization kinetics (see Figure S1 for the crystallization kinetics curve) with the A-E model, parameters including apparent rate constant  $k$ , induction time  $\vartheta$  and Avrami - Erofe'ev exponent  $n$  were extracted from the fitting results (see Table 1). Under the synthesis condition described in the experimental section, the induction time  $\vartheta$  is determined to be 0.81 h. As a result, the TEM image at  $t_c = 4$  h (see Figure 5) presents partially-crystallized morphology, because the sample has already experienced the induction period.<sup>51</sup>

**Table 1.** Avrami-Erofe'ev model parameters for *in situ* synthesis of zeolite X.

Parameter	$k$ ( $\text{h}^{-1}$ )	$\vartheta$ (h)	$n$	$R^2$
Value	0.16	0.81	1.93	0.99

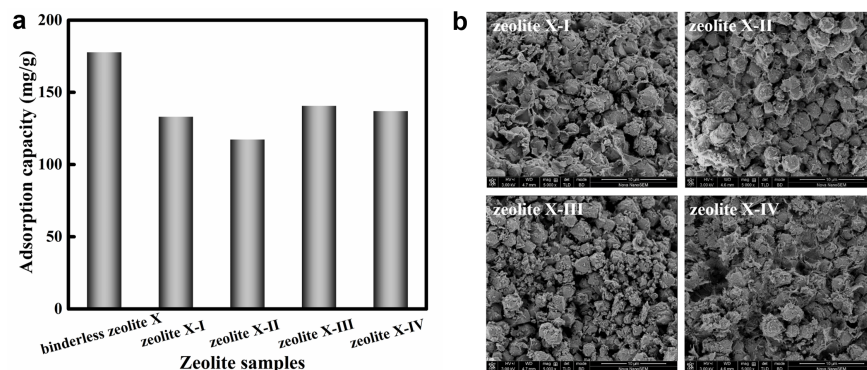


**Figure 7.** (a) 1-Hexene adsorption capacity on binderless zeolite X pellets and commercial binder-containing zeolite X samples. (b) SEM images of commercial binder-containing samples.

### 1-Hexene adsorption performance

1-Hexene gas phase adsorption was carried out to determine the adsorption capacity of the as-synthesized binderless zeolite X pellets. Several commercial binder-containing products were also tested as references (see Figure 7a). The 1-hexene adsorption capacity of synthesized binderless zeolite X sample is 20-35% higher than those of the four commercial binder-containing products, labeled as zeolite X-I – X-IV. Specifically, the adsorption capacities are 178.2 mg/g for the binderless zeolite X pellets, 133.6 mg/g for zeolite X-I, 117.9 mg/g for zeolite X-II, 141.2 mg/g for zeolite X-III, and 137.5 mg/g for zeolite X-IV. Compared with the final product synthesized at  $t_c = 24$  h (see Figure 4), the SEM images shown in Figure 7b reveal that the zeolite crystals of all binder-containing samples are covered with large amount of binder which has significantly negative impact in the adsorption performance, both capability and rate. Additionally, according to the pore

structure analysis results listed in Table S3, all binder-containing samples present smaller BET specific surface areas and total pore volumes compared with binderless zeolite X synthesized here. This can be ascribed to the dilution effect as well as filling of space among zeolite crystals and added binder species.<sup>35</sup> Therefore, the binderless zeolite X we synthesized is a promising candidate for adsorption of olefin compounds with significantly enhanced capacity and affinity.

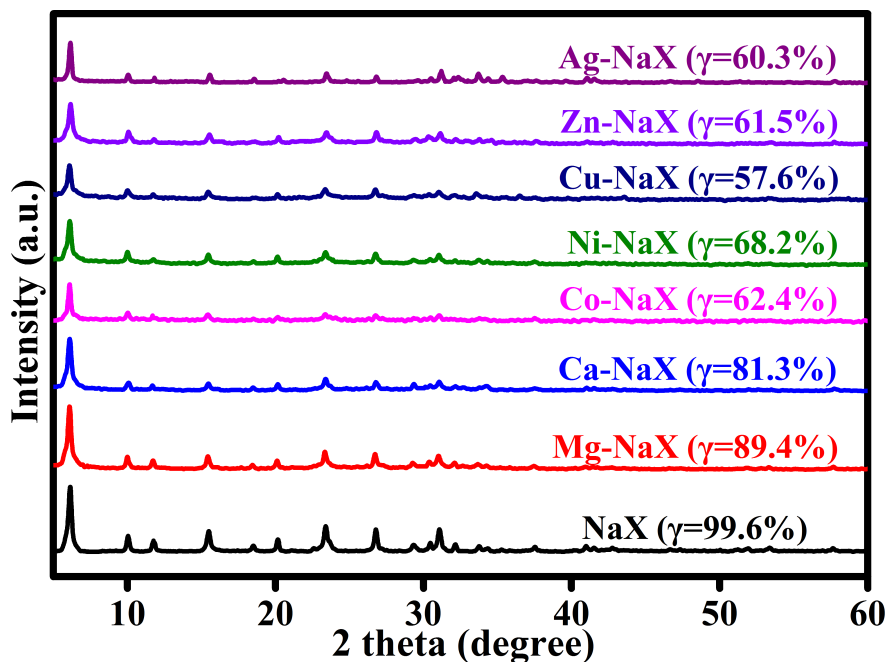


**Figure 8.** XRD patterns of different ion-exchanged zeolite X samples.

#### Tuning 1-hexene adsorption via ion-exchange of binderless zeolite NaX

To finetune the 1-hexene adsorption performance, we further modified the synthesized binderless zeolite NaX pellets by post-synthesis ion-exchange with a series of metal nitrate solutions. The chemical compositions of all ion-exchanged zeolite X samples are listed in Table S1. The XRD patterns in Figure 8 confirm that all ion-exchanged binderless samples share characteristic FAU topology. However, decrease in peak intensity due to crystallinity loss can be observed for all ion-exchanged samples. Similar findings have been reported previously.<sup>57</sup> Among these ion-exchanged samples, Mg-NaX and Ca-NaX present comparable XRD peak intensity as the parent NaX sample with relative crystallinity of 89.4 % (Mg-NaX) and 81.3 % (Ca-NaX), while Co-NaX, Cu-NaX, Zn-NaX and Ag-NaX exhibit crystallinity degradation of about 40 %, with relative crystallinity of 62.4 % (Co-NaX), 57.6 % (Cu-NaX), 61.5 % (Zn-NaX) and 60.3 % (Ag-NaX).

Introduction of  $\text{Co}^{2+}$ ,  $\text{Ni}^{2+}$ ,  $\text{Cu}^{2+}$ ,  $\text{Zn}^{2+}$  and  $\text{Ag}^+$  into the parent zeolite X decreases the BET specific surface area and overall pore volume (see Table S3). This is primarily caused by the degradation in crystallinity during ion-exchange, suggested by the XRD results. In contrast, incorporation of divalent  $\text{Mg}^{2+}$  and  $\text{Ca}^{2+}$  into zeolite X structure generates more free space when keeping the overall framework charge being balanced, leading to increased BET specific surface area and pore volume.<sup>58</sup> In addition, Mg-NaX and Ca-NaX show comparable crystallinity to that of the parent NaX, and decrease in molecular weight (see Table S1 for chemical compositions of different samples) also accounts for the change in pore structure analysis results on a weight basis.

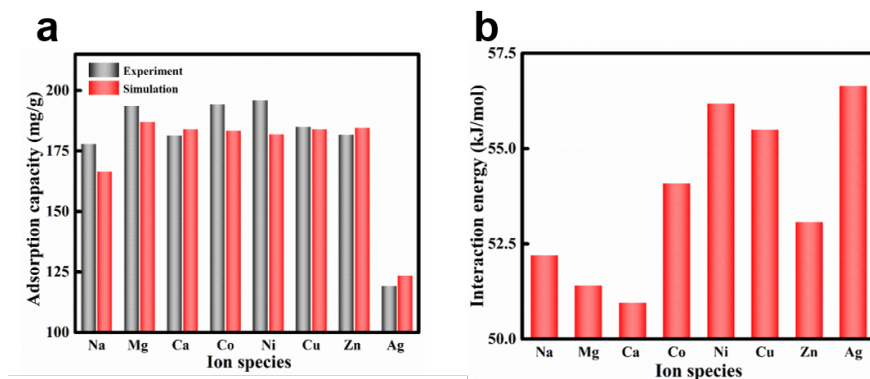


**Figure 9.** (a) Experimental and simulated 1-hexene adsorption capacity and (b) calculated 1-hexene – zeolite X interaction energies of all fully ion-exchanged zeolite X.

Gas phase adsorption of 1-hexene was carried out to evaluate the adsorption capacity of ion-exchanged zeolite X samples (see Figure 9a for the experiment results). Compared with the as-synthesized zeolite NaX (178.2 mg/g), six ion-exchanged samples have larger adsorption capacities. Specifically, they are 193.9 mg/g for Mg-NaX, 181.7 mg/g for Ca-NaX, 194.5 mg/g for Co-NaX, 196.2 mg/g for Ni-NaX, 185.2 mg/g for Cu-NaX and 182.0 mg/g for Zn-NaX. The enhanced adsorption capacities of Mg-NaX and Ca-NaX samples are ascribed to the decrease in molecular weight as well as the increased pore volume ( $0.313 \text{ cm}^3 \cdot \text{g}^{-1}$  for NaX,  $0.326 \text{ cm}^3 \cdot \text{g}^{-1}$  for Mg-NaX, and  $0.317 \text{ cm}^3 \cdot \text{g}^{-1}$  for Ca-NaX). Unlike Mg-NaX and Ca-NaX samples, the enhanced adsorption capacities of Co, Ni, Cu and Zn-exchanged samples are ascribed to the increase of adsorption centers ( $\pi$ -complexation) and interaction energy.<sup>30</sup> For Ag-NaX, a 23.4 % increase in molecular weight leads to significant decrease of 1-hexene adsorption capacity. Furthermore, we used GCMC simulation to calculate the adsorption of 1-hexene on these ion-exchanged zeolite X samples. The unit cell structures are presented in Figure S2. Overall, the simulation results are consistent with the experimental data for all ion-exchanged samples (see Figure 9a).

To further evaluate the effect of ion-exchange on adsorption performance, the van der Waals interaction energy between 1-hexene and zeolite was calculated by the Locate Task in the Sorption module of the Accelrys Package (see Figure 9b). The adsorption process was strictly restricted to feature one 1-hexene molecule confined in each zeolite X cage to exclude the intermolecular force among adsorbates. According to the GCMC simulation results, introduction of  $\text{Mg}^{2+}$  and  $\text{Ca}^{2+}$  into zeolite NaX frameworks leads to decreased interaction energies from 52.22 kJ/mol for NaX to 51.42 kJ/mol for Mg-NaX and 50.97 kJ/mol for Ca-

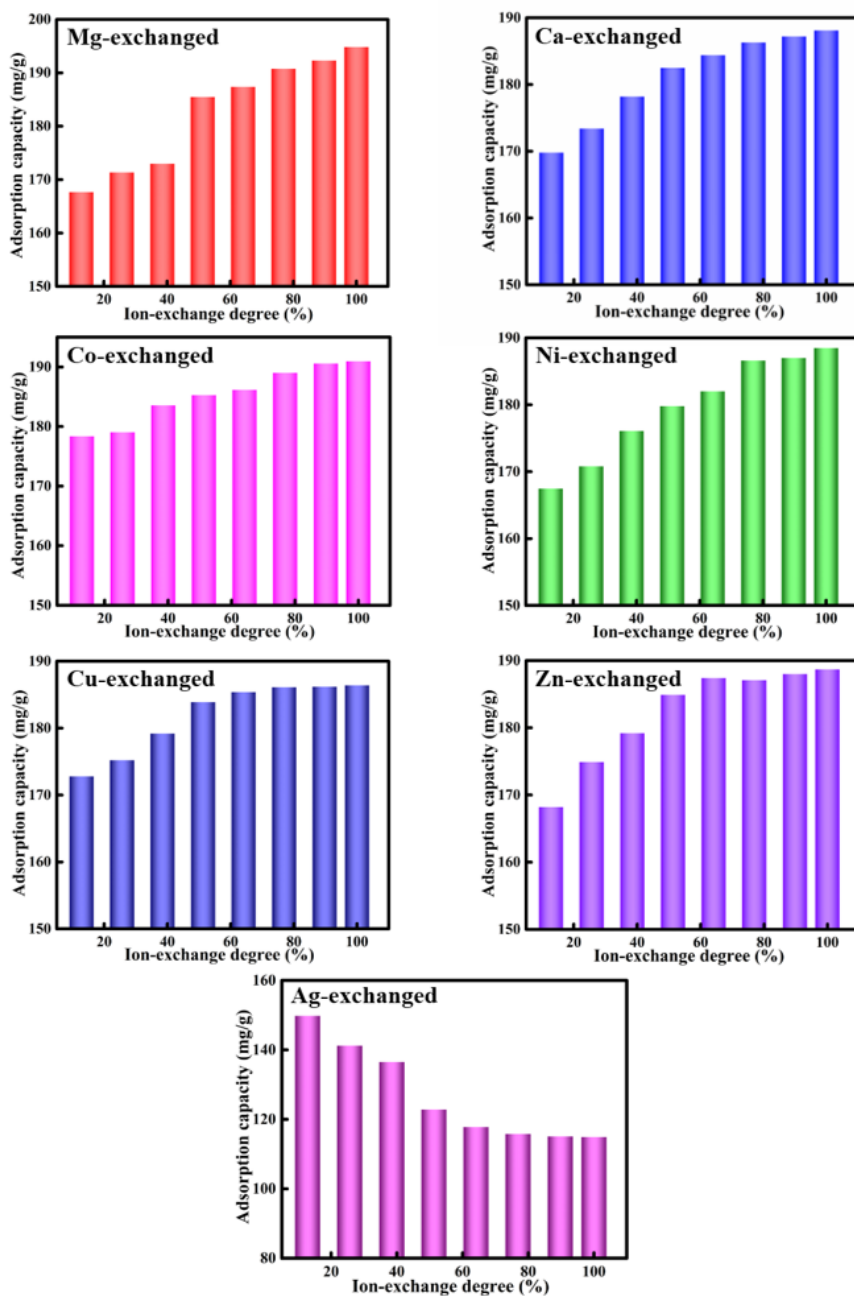


**Figure 10.** Calculated 1-hexene adsorption capacities on all ion-exchanged zeolite X samples.

NaX. Such phenomenon is due to decrease in the number of adsorption sites.<sup>59</sup> In contrast, ion-exchange of  $\text{Na}^+$  with  $\text{Co}^{2+}$ ,  $\text{Ni}^{2+}$ ,  $\text{Cu}^{2+}$ ,  $\text{Zn}^{2+}$  and  $\text{Ag}^+$  increases the 1-hexene – zeolite X interaction energies to 54.10 kJ/mol for Co-NaX, 56.20 kJ/mol for Ni-NaX, 55.51 kJ/mol for Cu-NaX, 53.09 kJ/mol for Zn-NaX, and 56.66 kJ/mol for Ag-NaX. Such enhancement is beneficial and will lead to more effective uptake of olefin from olefin/paraffin mixtures. Indeed, the enhanced guest – host interaction energies are due to  $\pi$ -complexation, which enables weak and reversible bonds between transition metal ions and olefin molecules, resulting in olefin/paraffin separation with better selectivity.<sup>60,61</sup> According to the calculated interaction

energies, compared with Co-NaX, Cu-NaX and Zn-NaX, the higher adsorption capacity seen on Ni-NaX may be enabled by the interplays between more favorable cation-substituted structure and larger interaction energy.

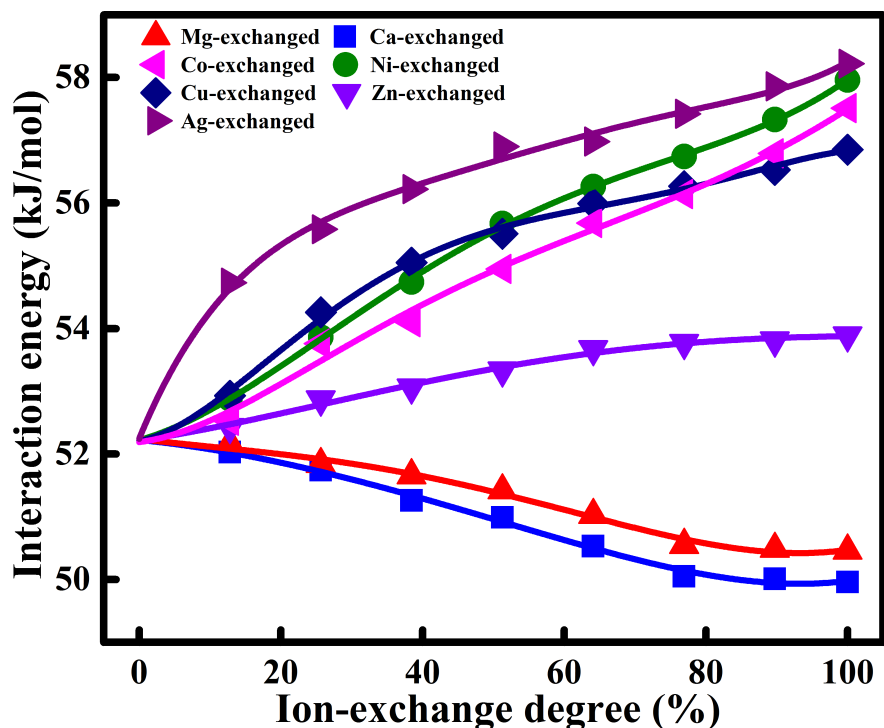


**Figure 11.** Calculated 1-hexene – zeolite interaction energies of ion-exchanged samples with different degrees of ion-exchange.

The adsorption properties of zeolite X samples with different ion-exchange degrees were calculated to further evaluate the effects of ion type and degree of ion-exchange (see Figures 10 and 11). In summary, introduction of  $\text{Mg}^{2+}$  and  $\text{Ca}^{2+}$  into zeolite X leads to increased adsorption capacity due to pore volume increase yet results in decrease in interaction energy. Indeed, such effect tends to be more significant as the degree of  $\text{Mg}^{2+}$  and  $\text{Ca}^{2+}$  exchange increases. In contrast, for Co-NaX, Ni-NaX, Cu-NaX and Zn-NaX, as ion-exchange proceeds, the magnitudes of both 1-hexene adsorption capacity and interaction energy increase. This is mainly caused by the  $\pi$ -complexation among 1-hexene molecules and transition metal ions. Moreover, the adsorption capacity of Ag-exchanged zeolite X decreases mainly due to the increase of molecular weight, while the magnitude of interaction energy increases owing to  $\pi$ -complexation. Generally, the impacts of ion-exchange degree on both adsorption capacity and interaction energy tend to be less significant as the ion-exchange reaches above 60%.

According to the calculated adsorption capacity, fully ion-exchanged MgX presents the highest adsorption capacity of 195.0 mg/g. Interestingly, at a low ion-exchange degree of 12.8%, Co-NaX shows a higher uptake (178.5 mg/g) as compared to other partially cation-replaced samples at the same exchange level. Additionally, full replacement of  $\text{Na}^+$  with  $\text{Ag}^+$  in zeolite X leads to a decreased adsorption capacity of 115.1 mg/g. We also found that the calculated 1-hexene – zeolite X interaction energy at the same ion-exchanged degree follow the transition metal electronegativity order of  $\text{Ag} > \text{Ni} > \text{Co} > \text{Cu} > \text{Zn} > \text{Mg} > \text{Ca}$ . This is because that in zeolite X framework transition metal ion with a greater electronegativity has stronger bonding with 1-hexene.<sup>61</sup> We also noticed that metals with very high electronegativity values lead to poor (incomplete) regeneration.

In summary, according to our experimental and simulation results, Mg-NaX, Ca-NaX, Co-NaX, Ni-NaX, Cu-NaX and Zn-NaX exhibit higher adsorption capacities, and exchange of  $\text{Co}^{2+}$ ,  $\text{Ni}^{2+}$ ,  $\text{Cu}^{2+}$ ,  $\text{Zn}^{2+}$  and  $\text{Ag}^+$  into zeolite X structure increases the interaction energy between 1-hexene and zeolite X. Ion-exchange enhances the adsorption performance of binderless zeolite X as a promising olefin/paraffin separation sorbent. On the other hand, our GCMC simulation provides experimental guidance to elucidate the relationships among ion type, exchange degree and adsorption performance. This study has significant implications for the controllable preparation of function-strengthened porous materials for adsorption and may benefit chemical engineers by providing fundamental knowledge governing the performance of zeolite-based olefin/paraffin separation materials.

## Conclusions

In this study, we demonstrate the feasibility of binderless zeolite X pellets synthesis using the one-pot synthesis method. Precursors with different synthesis periods were fully characterized by multiple techniques to investigate both the aging and crystallization mechanisms, and to derive the crystallization kinetics. According to our results, the formation of 4R and 6R in aging are through effective linking among diffused Al species and dissolved Si species. Subsequently, zeolite X is crystallized through reorganization of  $\beta$  cages with D6R. In addition, we predict the adsorption capacity and interaction energy of 1-hexene adsorption using ion-exchanged zeolite X with different ion species and degrees of exchange via GCMC simulation. Mg-NaX and Ca-NaX present higher 1-hexene uptake, and Co-NaX, Ni-NaX, Cu-NaX and Zn-NaX show enhanced adsorption capacity and increased binding affinity with degree of ion-exchange. All these data strongly suggest that the post-synthesis ion-exchanged binderless zeolite X samples we reported here have promising future to be applied as sorbents for the olefin/paraffin separation.

## Acknowledgements

This work is financially supported by the National Natural Science Foundation of China (Grant 91634112 and 21878097), SINOPEC (34400007-19-ZC0607-0117) and the Natural Science Foundation of Shanghai (Grant 16ZR1408100). D.W. acknowledges the institutional funds from the Gene and Linda Voiland School of Chemical Engineering and Bioengineering, and the Alexandra Navrotsky Institute for Experimental Thermodynamics at Washington State University.

## Literature Cited

1. Lin RB, Li LB, Zhou HL, Wu H, He CH, Li S, Krishna R, Li JP, Zhou W, Chen BL. Molecular sieving of ethylene from ethane using a rigid metal-organic framework. *Nat Mater.* 2018;17(12):1128-1133.
2. Bae YS, Lee CY, Kim KC, Farha OK, Nickias P, Hupp JT, Nguyen ST, Snurr RQ. High propene/propane selectivity in isostructural metal-organic frameworks with high densities of open metal sites. *Angew Chem Int Edit.* 2012;51(8):1857-1860.
3. Li KH, Olson DH, Seidel J, Emge TJ, Gong HW, Zeng HP, Li J. Zeolitic imidazolate frameworks for kinetic separation of propane and propene. *J Am Chem Soc.* 2009;131(30):10368-10369.
4. Hou JJ, Liu PC, Jiang MHZ, Yu L, Li LS, Tang ZY. Olefin/paraffin separation through membranes: from mechanisms to critical materials. *J Mater Chem A.* 2019;7(41):23489-23511.
5. Corma A, Melo FV, Sauvanaud L, Ortega F. Light cracked naphtha processing: Controlling chemistry for maximum propylene production. *Catal Today.* 2005;107: 699-706.
6. Ren T, Patel M, Blok K. Olefins from conventional and heavy feedstocks: Energy use in steam cracking and alternative processes. *Energy.* 2006;31(4):425-451.
7. Sholl DS, Lively RP. Seven chemical separations to change the world. *Nature.* 2016;532(7600):435-437.
8. Martins VFD, Ribeiro AM, Kortunov P, Ferreira A, Rodrigues AE. High purity ethane/ethylene separation by gas phase simulated moving bed using ZIF-8 adsorbent. *AIChE J.* 2019;65(8).

9. Chu S, Cui Y, Liu N. The path towards sustainable energy. *Nat Mater.* 2017;16(1):16-22.
10. Li RL, Xing HB, Yang QW, Zhao X, Su BG, Bao ZB, Yang YW, Ren QL. Selective extraction of 1-hexene against *n*-hexane in ionic liquids with or without silver salt. *Ind Eng Chem Res.*2012;51(25):8588-8597.
11. Bachman JE, Kapelewski MT, Reed DA, Gonzalez MI, Long JR.  $M_2$  (*m*-dobdc) (M= Mn, Fe, Co, Ni) metal-organic frameworks as highly selective, high-capacity adsorbents for olefin/paraffin separations. *J Am Chem Soc.*2017;139(43):15363-15370.
12. Martins VFD, Ribeiro AM, Santos JC, Loureiro JM, Gleichmann K, Ferreira A, Rodrigues AE. Development of gas-phase SMB technology for light olefin/paraffin separations. *AIChE J.* 2016;62(7):2490-2500.
13. Chen YW, Qiao ZW, Lv DF, Duan CX, Sun XJ, Wu HX, Shi RF, Xia QB, Li Z. Efficient adsorptive separation of  $C_3H_6$  over  $C_3H_8$  on flexible and thermoresponsive CPL-1. *Chem Eng J.* 2017;328:360-367.
14. Kwon HT, Jeong HK. In situ synthesis of thin zeolitic-imidazolate framework ZIF-8 membranes exhibiting exceptionally high propylene/propane separation. *J Am Chem Soc.*2013;135(29):10763-10768.
15. Bux H, Chmelik C, Krishna R, Caro J. Ethene/ethane separation by the MOF membrane ZIF-8: molecular correlation of permeation, adsorption, diffusion. *J Membrane Sci.* 2011;369(1-2):284-289.
16. Hong GH, Ji D, Kang SW. Highly permeable ionic liquid/Cu composite membrane for olefin/paraffin separation. *Chem Eng J.*2013;230:111-114.
17. Eldridge RB. Olefin/paraffin separation technology: a review. *Ind Eng Chem Res.* 1993;32(10):2208-2212.
18. Padin J, Rege SU, Yang RT, Cheng LS. Molecular sieve sorbents for kinetic separation of propane/propylene. *Chem Eng Sci.*2000;55(20):4525-4535.
19. Narin G, Martins VFD, Campo M, Ribeiro AM, Ferreira A, Santos JC, Schumann K, Rodrigues AE. Light olefins/paraffins separation with 13X zeolite binderless beads. *Sep Purif Technol.* 2014;133:452-475.
20. Liu JQ, Calverley EM, McAdon MH, Goss JM, Liu YJ, Andrews KC, Wolford TD, Beyer DE, Han CS, Anaya DA, Golombeski RP, Broomall CF, Sprague S, Clements H, Mabe KF. New carbon molecular sieves for propylene/propane separation with high working capacity and separation factor. *Carbon.* 2017;123:273-282.
21. Ma XL, Lin BK, Wei XT, Kniep J, Lin YS. Gamma-alumina supported carbon molecular sieve membrane for propylene/propane separation. *Ind Eng Chem Res.* 2013;52(11):4297-4305.
22. Cui WG, Hu TL, Bu XH. Metal-Organic Framework Materials for the Separation and Purification of Light Hydrocarbons. *Adv Mater.*2019;1806445.
23. Sun H, Ren DN, Kong RQ, Wang D, Jiang H, Tan JL, Wu D, Chen SW, Shen BX. Tuning 1-hexene/*n*-hexane adsorption on MOF-74 via constructing Co-Mg bimetallic frameworks. *Micropor Mesopor Mat.*2019;284:151-160.
24. Weckhuysen BM, Yu JH. Recent advances in zeolite chemistry and catalysis. *Chem Soc Rev.* 2015;44(20):7022-7024.
25. Brosillon S, Manero MH, Foussard JN. Mass transfer in VOC adsorption on zeolite: experimental and theoretical breakthrough curves. *Environ Sci Technol.* 2001;35(17):3571-3575.
26. Nouar F, Eckert J, Eubank JF, Forster P, Eddaoudi M. Zeolite-like metal-organic frameworks (ZMOFs) as hydrogen storage platform: lithium and magnesium ion-exchange and  $H_2$ -(*rho*-ZMOF) interaction studies. *J Am Chem Soc.* 2009;131(8):2864-2870.
27. Tan YX, He YP, Zhang J. Pore partition effect on gas sorption properties of an anionic metal-organic framework with exposed  $Cu^{2+}$  coordination sites. *Chem Commun.*2011;47(38):10647-10649.

28. Sakai M, Sasaki Y, Tomono T, Seshimo M, Matsukata M. Olefin Selective Ag-Exchanged X-Type Zeolite Membrane for Propylene/Propane and Ethylene/Ethane Separation. *ACS Appl Mater Inter.*2019;11(4):4145-4151.
29. Anson A, Wang Y, Lin CCH, Kuznicki TM, Kuznicki SM. Adsorption of ethane and ethylene on modified ETS-10. *Chem Eng Sci.*2008;63(16):4171-4175.
30. Abreu NJ, Valdés H, Zaror CA, Azzolina-Jury F, Meléndrez MF. Ethylene adsorption onto natural and transition metal modified Chilean zeolite: An operando DRIFTS approach. *Micropor Mesopor Mat.*2019;274:138-148.
31. Silva JAC, Schumann K, Rodrigues AE. Sorption and kinetics of CO<sub>2</sub> and CH<sub>4</sub> in binderless beads of 13X zeolite. *Micropor Mesopor Mat.* 2012;158:219-228.
32. Fakin T, Ristić A, Mavrodinova V, Logar NZ. Highly crystalline binder-free ZSM-5 granules preparation. *Micropor Mesopor Mat.*2015;213:108-117.
33. Schumann K, Unger B, Brandt A, Scheffler F. Investigation on the pore structure of binderless zeolite 13X shapes. *Micropor Mesopor Mat.* 2012;154:119-123.
34. Mehlhorn D, Valiullin R, Kärger J, Schumann K, Brandt A, Unger B. Transport enhancement in binderless zeolite X- and A-type molecular sieves revealed by PFG NMR diffusometry. *Micropor Mesopor Mat.*2014;188:126-132.
35. Sun H, Sun ZW, Shen BX, Liu JC, Li GN, Wu D, Zhang YX. One-pot synthesis of binderless zeolite A spheres via in situ hydrothermal conversion of silica gel precursors. *AIChE J.*2018;64(11):4027-4038.
36. Accelrys. *Materials Studio, Modeling Getting Started.*Accelrys Software Inc.: San Diego, CA. 2004.
37. Lowenstein W. Apparatus for Separating Fluorine from Aluminosilicates by Pyrohydrolysis. *Am Mineral.* 1954;39:92.
38. Park HJ, Suh MP. Enhanced isosteric heat, selectivity, and uptake capacity of CO<sub>2</sub> adsorption in a metal-organic framework by impregnated metal ions. *Chem Sci.* 2013;4(2):685-690.
39. Jale SR, Bülow M, Fitch FR, Perelman N, Shen D. Monte Carlo simulation of sorption equilibria for nitrogen and oxygen on LiLSX zeolite. *J Phys Chem B.* 2000;104(22):5272-5280.
40. Zhu L, Seff K. Reinvestigation of the crystal structure of dehydrated sodium zeolite X. *J Phys Chem B.* 1999;103(44):9512-9518.
41. Nath SK, Banaszak BJ, de Pablo JJ. A new united atom force field for  $\alpha$ -olefins. *J Chem Phys.* 2001;114(8):3612-3616.
42. Calero S, Dubbeldam D, Krishna R, Smit B, Vlugt TJH, Denayer JFM, Martens JA, Maesen TLM. Understanding the role of sodium during adsorption: A force field for alkanes in sodium-exchanged faujasites. *J Am Chem Soc.* 2004;126(36):11377-11386.
43. Sun H. COMPASS: an ab initio force-field optimized for condensed-phase applications overview with details on alkane and benzene compounds. *J Phys Chem B.* 1998;102(38):7338-7364.
44. Jirapongphan SS, Warzywoda J, Budil DE, Jr SA. Simulation of benzene adsorption in zeolite HY using supercage-based docking. *Micropor Mesopor Mat.* 2006;94:358-363.
45. Dang SQ, Zhao L, Gao JS, Xu CM. Loading dependence of the adsorption mechanism of thiophene in FAU zeolite. *Ind Eng Chem Res.*2016;55(45):11801-11808.
46. Garaga MN, Persson M, Yaghini N, Martinelli A. Local coordination and dynamics of a protic ammonium based ionic liquid immobilized in nano-porous silica micro-particles probed by Raman and NMR spectroscopy. *Soft Matter* . 2016;12(9):2583-2592.

47. Dutta PK, Twu J. Influence of framework Si/Al ratio on the Raman spectra of faujasitic zeolites. *J Phys Chem.*1991;95(6):2498-2501.
48. Sharma SK, Mammone JF, Nicol MF. Raman investigation of ring configurations in vitreous silica. *Nature.*1981;292(5819):140-141.
49. Dutta PK, Shieh DC, Puri M. Raman spectroscopic study of the synthesis of zeolite Y. *J Phys Chem.* 1987;91(9):2332-2336.
50. Xiong G, Yu Y, Feng ZC, Xin Q, Xiao FS, Li C. UV Raman spectroscopic study on the synthesis mechanism of zeolite X. *Micropor Mesopor Mat.* 2001;42(2-3):317-323.
51. Fan FT, Feng ZC, Li GN, Sun KJ, Ying PL, Li C. In situ UV Raman spectroscopic studies on the synthesis mechanism of zeolite X. *Chem Eur J.* 2008;14(17):5125-5129.
52. Yu Y, Xiong G, Li C, Xiao FS. Characterization of aluminosilicate zeolites by UV Raman spectroscopy. *Micropor Mesopor Mat.*2001;46(1):23-34.
53. Lippmaa E, Mägi M, Samoson A, Tarmak M, Engelhardt G. Investigation of the structure of zeolites by solid-state high-resolution  $^{29}\text{Si}$  NMR spectroscopy. *J Am Chem Soc.*1981;103(17):4992-4996.
54. Ma YN, Yan CJ, Alshameri A, Qiu XM, Zhou CY, Li D. Synthesis and characterization of 13X zeolite from low-grade natural kaolin. *Adv Powder Technol.* 2014;25(2): 495-499.
55. Finney EE, Shields SP, Buhro WE, Finke RG. Gold nanocluster agglomeration kinetic studies: evidence for parallel bimolecular plus autocatalytic agglomeration pathways as a mechanism-based alternative to an avrami-based analysis. *Chem Mater.* 2012;24(10):1718-1725.
56. Zhang RH, Li XK, Cao GP, Shi YH, Liu HL, Yuan WK, Roberts GW. Improved kinetic model of crystallization for isotactic polypropylene induced by supercritical  $\text{CO}_2$ : introducing pressure and temperature dependence into the avrami equation. *Ind Eng Chem Res.* 2011;50(18):10509-10515.
57. Chen X, Shen BX, Sun H, Zhan GX, Huo ZZ. Adsorption and its mechanism of  $\text{CS}_2$  on ion-exchanged zeolites Y. *Ind Eng Chem Res.* 2017;56(22):6499-6507.
58. Chen X, Shen BX, Sun H, Zhan GX. Ion-exchange modified zeolites X for selective adsorption desulfurization from Claus tail gas: Experimental and computational investigations. *Micropor Mesopor Mat.* 2018;261:227-236.
59. Zhang JF, Burke N, Yang YX. Molecular Simulation of Propane Adsorption in FAU Zeolites. *J Phys Chem C.*2012;116(17):9666-9674.
60. Dewar MJS. *Α ρεινω οφ τηε π-ζομπλεξ τηεορψ* . Bulletin de la Socie'te' Chimique, France. 1951;18(3-4):C71-C79.
61. Faiz R, Li K. Olefin/paraffin separation using membrane based facilitated transport/chemical absorption techniques. *Chem Eng Sci.* 2012;73(21):261-284.